Detecting Gaussian Signals Using Coprime Sensor Arrays in Spatially Correlated Gaussian Noise

Radienxe Bautista, *Member, IEEE*, and John R. Buck, *Senior Member, IEEE*

***Abstract*—Coprime sensor arrays (CSAs) can estimate the directions of arrival of O(MN) narrowband planewave sources using only O(M + N) sensors with the CSA product processor. All previous investigations on the product processed CSA's performance for detecting Gaussian signals assumed spatially white Gaussian noise. Considering the product and conventional delay-and-sum beamforming processors applied to the CSA geometry, this paper derives the detection gain for each processor under the deflection metric when the background noise is spatially correlated. The conditional probability distribution functions are also derived in closed form to evaluate and compare the receiver operating characteristic performances. Despite the nonlinear processing, the product processed CSA's detection performance closely rivals its conventional beamforming (CBF) counterpart, while also demonstrating greater robustness than the CBF to spatially correlated Gaussian noise.**

***Index Terms*—Coprime sensor arrays, sparse arrays, spatially correlated Gaussian noise, detection performances, Gaussian signal detection, receiver operating characteristic analysis, detection gain, deflection criterion.**

I. Introduction

COPRIME sensor arrays (CSAs) offer the attractive capability of estimating $\mathcal{O}(MN)$ directions of arrival (DoAs) for narrowband planewave sources from only $\mathcal{O}(M+N)$ sensors [1]. A CSA interleaves two undersampled uniform line arrays (ULAs) to create a sparse array. Compared to a filled ULA with the same number of sensors spaced every half wavelength, a CSA with $\mathcal{O}(M+N)$ sensors spans a larger aperture of $\mathcal{O}(MN)$, achieving better spatial resolution. Even though the CSA is a sparse array, the CSA's difference coarray [2], [3] includes a large hole-free region of width $\mathcal{O}(MN)$ [1], [4], [5]. This large hole-free region in the coarray indicates that one can create a large Toeplitz augmented covariance matrix (ACM) by shuffling the entries in the sample covariance matrix (SCM) [6], [7], possibly supplemented by averaging and smoothing [8]. Processing this ACM with subspace DoA estimators such as MUSIC [9] yields DoA estimates for up to $\mathcal{O}(MN)$ sources. A major design goal for sparse arrays is reducing the redundancy for each lag in the difference coarray [3], [10], [11] resulting in relatively few independent measurements contributing to each covariance estimate in the ACM. This makes these correlation estimates susceptible to noise. Every published analysis and simulation of CSA performance to date assumes spatially white background noise [1], [4], [5], [12]–[20], although many real world array processing scenarios include a significant component of spatially correlated noise. How CSA processors perform in spatially correlated noise fields remains an important but previously unexplored question.

This paper examines how spatially correlated noise impacts the detection performance of the CSA augmented covariance processing technique originally proposed for these arrays in Ref. [1]. This "product processing" technique based on multiplying the subarray scanned responses, is denoted CSA_{pp} below. We quantify the CSA_{pp} detection performance as a function of the noise's spatial correlation scale on two levels. First, we compute the deflection statistic [21]–[27], as a scalar metric summarizing the detection gain. Operationally speaking, detection gain measures how much the average single sensor SNR must increase so that a detector processing that single sensor achieves comparable detection performance to the array output. For a linear detector, the detection gain equals the classic definition of array gain, which is the ratio of the array output SNR to the average sensor input SNR. However, for nonlinear detectors like CSA_{pp}, or scenarios with limited or unknown coherence issues, the deflection statistic is a more appropriate measure of detection gain than the classic array gain [24], [27].* Second, we compute the Receiver Operating Characteristic (ROC) [21] as a more complete characterization of detection performance, quantifying the tradeoff between detection and false alarms with varying detector thresholds.

To place the performance of the CSA_{pp} in context, we compare the detection performance of the CSA_{pp} with two other array processors. The first comparison, denoted CSA_{cbf} below, processes the same CSA geometry with conventional beamforming (CBF) as a single coherent nonuniform line array instead of two uniform subarrays. The second comparison, denoted ULA_{cbf}, is with a filled CBF ULA containing the same number of sensors as the CSA. This ULA will have significantly

Manuscript received February 20, 2018; revised September 17, 2018 and November 30, 2018; accepted December 1, 2018. Date of publication January 1, 2019; date of current version January 15, 2019. The associate editor coordinating the review of this manuscript and approving it for publication was Prof. Yimin D. Zhang. This work was supported by the Naval Undersea Warfare Center (NUWC) Naval Innovative Science and Engineering (NISE) 219 program, and by the ONR Basic Research Challenge Program Grants N00014-13-1-0230 and N00014-17-1-2397. *(Corresponding author: Radienxe Bautista.)*

R. Bautista is with the Sensors and Sonar Department, Naval Undersea Warfare Center, Newport, RI 02841 USA (e-mail: radienxe.bautista@navy.mil).

J. R. Buck is with the Department of Electrical and Computer Engineering, University of Massachusetts Dartmouth, North Dartmouth, MA 02747 USA (e-mail: johnbuck@ieee.org).

Digital Object Identifier 10.1109/TSP.2018.2887399

*Characterizing the performance of a nonlinear processor like CSA_{pp} or a split beam processor [23], [28] with the standard array gain definition may lead to paradoxical and confusing results, like a white noise gain that exceeds the number of sensors in the array.

less aperture than the CSA, sacrificing spatial resolution. The filled ULA avoids the grating lobes and high sidelobes common in nonuniform line arrays [10, Sec 3.3.5] [29, Ch. 7 and 8]. There are two choices for comparing the performance of sparse arrays with filled ULAs: equal aperture or equal numbers of sensors [10, Sec 3.3.5]. This study focuses on detection performance, so we focus most of our work comparing the sparse CSA with a filled ULA with an equal number of sensors. Although this choice results in a much smaller aperture and degraded spatial resolution for the ULA, equal sensors is the more appropriate comparison when focusing on the detection context, since this constraint ensures both detectors have the same number of measurements available.

All three detectors compared in this paper employ CBF for narrowband planewaves arriving from the direction of interest. CBF is equivalent to a spatial matched filter for planewave signals, and thus is the optimal detector for a single planewave in spatially white noise. For the ULA_{cbf} and CSA_{cbf}, the CBF operates on the full array aperture as a single coherent array, and the detector statistic is the power of the CBF output. For the CSA_{pp}, the CBF processes each subarray separately, and the detector statistic is the magnitude of the product of these subarray outputs [14]. CBF is often used in detectors operating in unknown or varying spatially correlated noise environments due to its robustness to mismatch in array elements' locations, gains and phase responses [30]. A few studies have examined the performance of linear and quadratic detectors for ULAs when the signal suffers from fading coherence in white noise [23], [27]. The case studied here, however, is for coherent signals observed by sparse arrays in correlated noise.

The subspace DoA estimation algorithms exploited by CSA_{pp} processing assume an accurate estimate of the number of sources present in the data. This estimate can be obtained either by model order estimators [31]–[35] or by detecting peaks in an estimate of the spatial power spectral density (PSD), also known as the scanned response. The ACM is not Wishart distributed in general, implying existing model order estimators [31]–[34] are not suited for estimating the number of sources as they are for a ULA [36], [37]. Lacking appropriate statistical models for model-order estimators, the performance of the CSA_{pp} detector is consequently important to the overall performance of subspace DoA methods, although relatively few authors have studied it. Ref. [14] derived the conditional PDFs for the CSA_{pp} detector for signals in spatially white noise, and found that the detection gain asymptotically converges to the number of sensors in the high SNR and large coprime factor limits. Refs. [16]–[18] all proposed variants on order statistics to estimate the PSD for detecting planewave sources from CSA data. Ref. [16] derived the complementary cumulative distribution function (CCDF) for the "min" processor (CSA_{min}) for signals in the presence of interferers and white noise, and computed the ROC from the CCDF. These results found that the CSA_{min} processor improved performance detecting weak sources in the presence of loud interferers. Ref. [18] proposed a hybrid detector that combined the CSA_{pp} with the CSA_{min}, which further improved the hybrid detector's robustness over the individual processors in environments with many interferers. Again, all of these authors have limited their investigations to the spatially white noise case in contrast with the spatially correlated noise case considered here.

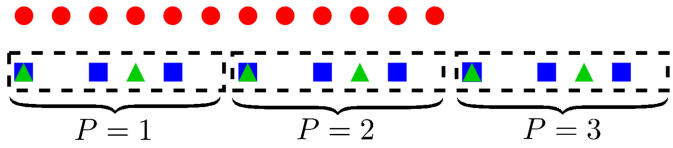

Fig. 1. ULA (red circles) compared to a CSA with the same number of sensors $L = \mathcal{I}_{csa} = 12$. Blue squares indicate sensors for the subarray undersampled by $M = 2$, green triangles for the subarray undersampled by $N = 3$. The extended CSA concatenates the "basic" geometry (dashed box), shown here for $P = 3$ periods. For the same number of sensors, the CSA has greater aperture than the ULA.

The paper is organized as follows. Section II models the input signal and the spatially correlated noise. Section III derives the output correlated noise powers to find the detection gains through the deflection statistic. Section IV evaluates the ROCs of each beamformer. Section V concludes the paper with a discussion of the results.

Notation and Conventions: This paper considers the discrete spatial signal obtained by sampling a narrowband spatial field $x_c(z)$ with omni-directional sensors along the z-axis on an underlying $\lambda_o/2$ grid, i.e., $x_d[l] = x_c(z = l\lambda_o/2)$, where λ_o is the design wavelength. The directional sine, $u = \sin(\theta)$, is used to represent DoA for this paper, and broadside is $u = \sin(0) = 0$. For the purposes of brevity and clarity, functions concerning the ULA_{cbf} will be subscripted with ula, e.g., $\kappa_{ula}[\gamma]$. For the CSA subarrays processed with the CBF, which are defined as ULAs undersampled by M or N, functions will be subscripted with the undersampling factor. For the CSA_{pp}, functions will be subscripted with the array geometry, csa, and superscripted with the processor pp, e.g., $\kappa_{csa}^{pp}[\gamma]$. A similar convention will be followed for the CSA_{cbf}, with the change in the superscript to cbf.

A. Array Geometries

The ULA aperture function, composed of L sensors with spacing $d = \lambda_o/2$, is defined as a set of Kronecker delta impulses to represent sensors arranged on a line, formally defined for this paper as $\iota_{ula}[l] = \sum_{i=0}^{L-1} \delta[l - i]$. The "basic" CSA geometry is composed of two subarrays having element spacings of $M\lambda_o/2$ and $N\lambda_o/2$ composed of N and M sensors respectively, sharing the first sensor, and M and N are coprime [1]. The extended CSA geometry concatenates P periods of the basic CSA, and is comparable in aperture to a filled ULA of $L = MNP$ sensors [13]. These geometries are shown in Fig. 1 for CSA parameters of $M = 2$, $N = 3$ and $P = 3$, and a ULA composed of the same number of 12 sensors. The extended CSA is composed of a total number of sensors $\mathcal{I}_{csa} = P(N + M - 1) = \mathcal{I}_M + \mathcal{I}_N - P$, and $\mathcal{I}_M = NP$ and $\mathcal{I}_N = MP$ are the number of sensors in each extended subarray. Similar to the ULA, a CSA subarray aperture function is defined as a uniformly spaced, zero-filled impulse train, e.g., $\iota_M[l] = \sum_{m=0}^{\mathcal{I}_M - 1} \delta[l - mM]$. The CSA aperture function will simply be a union of the undersampled subarrays, less the shared sensors to ensure a value of 1 at these locations, $\iota_{csa}[l] = \iota_M[l] + \iota_N[l] - \sum_{q=0}^{P-1} \delta[l - qMN]$. When

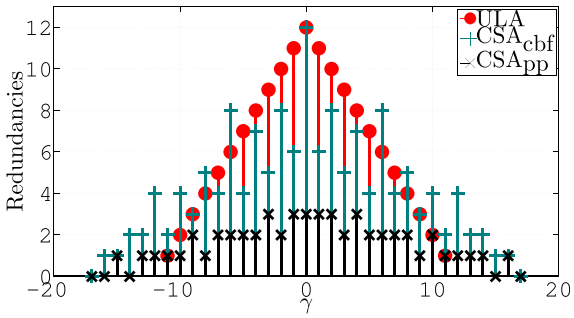

Fig. 2. Difference coarrays $\kappa_{ula}[\gamma]$ (red $-\circ$), $\kappa_{csa}^{cbf}[\gamma]$ (teal $-+$), $\kappa_{csa}^{pp}[\gamma]$ (black $-\times$) for the geometries shown in Fig. 1. The underlying spatial covariance function is windowed differently when estimated by the two processors for the same CSA [10, Sec 3.3.5]. Note, $\kappa_{ula}[0] = L$, $\kappa_{csa}^{cbf}[0] = \mathcal{I}_{csa}$, $\kappa_{csa}^{pp}[0] = P$.

convenient for linear algebra formulations the function $\iota[l]$ is represented by the vector $\boldsymbol{\iota}$, where the subscripts indicate which aperture indicator function is intended, e.g., $\boldsymbol{\iota}_{csa}$.

B. Difference Coarrays

For array geometries such as the ULA or the minimum redundancy array, the standard difference coarray is generated by auto-correlating the aperture sampling function [11] [10, Sec 3.3]. The ULA_{cbf} coarray $\kappa_{ula}[\gamma] = \sum_{l=0}^{L-1} \iota_{ula}[l]\iota_{ula}[l-\gamma]$ is a discrete triangle function known as the Bartlett window [10], [15], [38], [39]. The CSA_{cbf} treats the CSA as a single, non-uniform array and processes the array data with conventional beamforming, and its coarray is defined as $\kappa_{csa}^{cbf}[\gamma] = \sum_{l=0}^{MNP-1} \iota_{csa}[l]\iota_{csa}[l-\gamma]$.

The relevant function for sparse array processors, such as the CSA_{pp} and the nested array, is the cross-difference coarray [1]. The CSA_{pp} coarray is obtained by cross-correlating the subarray aperture functions embedded in its processor, $\kappa_{csa}^{pp}[\gamma] = \sum_{l=0}^{MNP-1} \iota_M[l]\iota_N[l-\gamma]$. Fig. 2 shows the coarrays for the example geometries in Fig. 1.

II. Input Signal and Correlated Noise Model

Many real world signal processing environments include spatially correlated noise. A primary goal of this paper is to eliminate the spatially white noise assumption used in previous studies of CSA performance. Studies such as Refs. [40]–[43] developed models for spatial correlation in the ocean caused by surface generated noise. Ref. [44] analyzed experimental data to study the spatial correlation caused by the turbulence caused by towed arrays. This paper explores the impact of spatially correlated noise on the detection performance of a CSA.

The input signal is modeled in a linear form,

$$\mathbf{x} = s\mathbf{v}_s + \boldsymbol{c} \tag{1}$$

where $\mathbf{v}_s = \exp(-j\pi l u_s)$ for $0 \le l < L-1$ is the planewave replica vector for a filled ULA with intersensor spacing $d = \lambda_o/2$ for a source arriving from u_s, and the amplitude is complex Gaussian distributed $s \sim \mathcal{CN}(0, \sigma_S^2)$. We will assume the signal arrives from broadside $u_s = 0$. The correlated noise component $\boldsymbol{c}$ is not correlated with s, but with itself across the array. The noise is assumed wide-sense stationary and is modeled as a first-order auto-regressive (AR) process that filters independent, identically distributed Gaussian noise $\mathbf{n} \sim \mathcal{CN}(\mathbf{0}, \sigma_W^2 \boldsymbol{I})$,

$$c[l] = \left(\sqrt{1-\alpha^2}\right) n[l] + (\alpha)\, c[l-1], 0 \le \alpha < 1 \tag{2}$$

where α is the adjacent sensor correlation between sensors separated by $\lambda_o/2$. The AR noise ensemble correlation function decays exponentially as sensor pairs become more separated,

$$r_{cc}[\gamma] = E\{c[l]c^*[l-\gamma]\} = \sigma_W^2\ \alpha^{|\gamma|}. \tag{3}$$

By convention, $0^0 = 1$, so for the case of $\alpha = 0$, $r_{cc}[\gamma] = \sigma_W^2\, \delta[\gamma]$, the spatially white noise ensemble correlation function. The sensor level input SNR for this signal model is σ_S^2/σ_W^2 [†].

III. Detection Gain

Detection gain (DG) measures the improvement in detection performance at the array processor output with respect to the detection performance at a single sensor. Similarly, it is the increase in SNR at a single sensor to achieve comparable detection performance as the beamformer from just one sensor. For coherent linear processors, the detection gain is simply the standard definition of array gain as the ratio of output SNR to input SNR, i.e., $\text{DG} = \text{SNR}_{out}/\text{SNR}_{in}$ [3]. For these processors, this SNR improvement fully quantifies the improvement in detection performance. However, for nonlinear processors like the CSA_{pp} or split beam sonar [23], the ratio of SNRs definition yields misleading or paradoxical results that fail to represent accurately the detection performance of the processor. Nonlinear processors require a more general definition for DG, the deflection criterion [21]–[26],

$$\text{DG} = \frac{E\{\check{y}|H_1\} - E\{\check{y}|H_0\}}{\sqrt{E\{\check{y}^2|H_0\} - E^2\{\check{y}|H_0\}}} \left(\frac{\sigma_W^2}{\sigma_S^2}\right). \tag{4}$$

The test statistic $\check{y}$ is the beamformer output for the different scenarios compared defined in detail below. The "deflection" measures the separation in the means of the conditional PDFs normalized by the standard deviation of the null hypothesis [21], [22].

The deflection as defined in (4) has been generalized for processors that are noncoherent or involve nonlinear processing of the array measurements [23]. The actual "deflection" has been interpreted as the "output SNR" [24]–[26]. For coherent linear processors like the CBF, the deflection statistic reassuringly converges to the familiar ratio of output to input SNR traditionally used to quantify DG for such processors. The CSA_{pp} output is nonlinear and similar in structure to the split-beam processor in [23], so the deflection is a more appropriate measure of detection performance.

A. Beamformer Output

All three processors compute a CBF output, either for the full aperture (ULA_{cbf} and CSA_{cbf}) or for uniformly spaced subar-

[†] Scaling by $\sqrt{1-\alpha^2}$ in (2) guarantees the correlated noise power $\sigma_c^2 = \sigma_W^2$ at a single sensor, and is independent of α (since the noise correlation would not necessarily impact the sensor level noise power in the physical sense) [45]. For completeness, the general AR noise component is complex Gaussian distributed $\boldsymbol{c} \sim \mathcal{CN}(\mathbf{0}, \sigma_W^2\, \boldsymbol{R}(\alpha))$, where the ensemble correlation matrix is Hermitian Toeplitz. Each entry of the matrix is $\boldsymbol{R}_{a,b}(\alpha) = \alpha^{|a-b|} = \alpha^{|\gamma|}$, and $\boldsymbol{R}(0) = \boldsymbol{I}$

rays (CSA_{pp}). The output of a CBF array steered to the signal direction is

$$y = \mathbf{w}^H \mathbf{x} = \mathbf{w}^H (s\mathbf{v}_s + \boldsymbol{c}) = s + \varsigma \tag{5}$$

where $\mathbf{w} = \mathbf{v}_s \odot \boldsymbol{\iota}/\mathcal{I}$ is the array steering vector, composed of the planewave replica vector element-wise multiplied with the aperture function of interest $\boldsymbol{\iota}$ (previously defined in Section I-A), and normalized by $\mathcal{I}$, the number of sensors in the geometry such that $\mathbf{w}^H \mathbf{v}_s = 1$ for any geometry. The beamformer output is $\check{y} = y_1 y_2^* = s_1 s_2^* + s_1 \varsigma_2^* + \varsigma_1 s_2^* + \varsigma_1 \varsigma_2^*$, where the subscripts on y indicate the "subarray" geometries embedded in the processor. The output for each beamformer is $\check{y}_{ula} = y_{ula} y_{ula}^*$, $\check{y}_{csa}^{cbf} = y_{csa} y_{csa}^*$, $\check{y}_{csa}^{pp} = y_M y_N^*$.

The moments of each output component are required to find the deflection. The output signal power is $E\{s_1 s_2^*\} = \sigma_S^2$. The cross-terms $E\{s_1 \varsigma_2^*\}$ and $E\{\varsigma_1 s_2^*\}$ go to zero because the signal and noise are independent and zero-mean. The expected power given the signal is present is $E\{\check{y}|H_1\} = \sigma_S^2 + E\{\varsigma_1 \varsigma_2^*\} = \sigma_S^2 + E\{\text{ONP}(\alpha)\}$, where the output noise power as a function of the correlation is $\text{ONP}(\alpha) \triangleq \varsigma_1 \varsigma_2^*$.

The noise contribution at the beamformer output is Gaussian distributed $\varsigma = \mathbf{w}_s^H \boldsymbol{c} \sim \mathcal{CN}(0, E\{\text{ONP}(\alpha)\})$. The correlated noise variance $E\{\text{ONP}(\alpha)\}$, corresponding to $E\{\check{y}|H_0\}$, is found through the perspective of coarray processing. The expected auto-correlation estimate is generally $E\{\hat{r}[\gamma]\} = r_{xx}[\gamma]\kappa[\gamma]/\mathcal{I}_1\mathcal{I}_2$ [10], [15]. The measured wavefield ensemble correlation function $r_{xx}[\gamma] = E\{x[l]x^*[l-\gamma]\}$ is windowed (or similarly sampled) by the coarray function of the array processor $\kappa[\gamma]$, (previously defined in Section I-B). Exploiting Fourier transform properties, the expected AR noise power at the signal direction $u_s = 0$ as a function of the correlation α is found by summing over the AR noise ensemble correlation function $r_{cc}[\gamma]$ windowed by the coarray, simplifying to

$$E\{\varsigma_1 \varsigma_2^*\} = E\{\text{ONP}(\alpha)\} = \sigma_W^2 \frac{1}{\mathcal{I}_1\mathcal{I}_2} \sum\nolimits_\gamma \alpha^{|\gamma|}\kappa[\gamma]. \tag{6}$$

The output SNR for a beamformer is

$$\text{SNR}_{out} = \frac{E\{s^2\}}{E\{\text{ONP}(\alpha)\}} = \left(\frac{\sigma_S^2}{\sigma_W^2}\right) \frac{\mathcal{I}_1\mathcal{I}_2}{\sum_\gamma \alpha^{|\gamma|}\kappa[\gamma]}. \tag{7}$$

B. Detection Gain for the ULA_{cbf} and the CSA_{cbf}

For a given array processed with the CBF, the output SNR is found by substituting into (7) the appropriate normalization ($\mathcal{I}_1\mathcal{I}_2 = L^2$ for the ULA_{cbf}, $\mathcal{I}_1\mathcal{I}_2 = \mathcal{I}_{csa}^2$ for the CSA_{cbf}), and the corresponding coarray function. The DG as a function of spatial correlation $0 \le \alpha < 1$ is

$$\text{DG}_{ula}(\alpha) : L \ge \frac{L^2}{\sum_\gamma \alpha^{|\gamma|}\kappa_{ula}[\gamma]} > 1$$

$$\text{DG}_{csa}^{cbf}(\alpha) : \mathcal{I}_{csa} \ge \frac{\mathcal{I}_{csa}^2}{\sum_\gamma \alpha^{|\gamma|}\kappa_{csa}^{cbf}[\gamma]} > 1. \tag{8}$$

Since the deflection converges to the ratio of SNRs for the linear CBF energy process, the DGs were proportional to (7). Both geometries have DGs with similar behavior. For white noise $\alpha = 0$, the sum in the denominator reduces to $\sum_\gamma \delta[\gamma]\kappa[\gamma] = \kappa[0] = \mathcal{I}$, which results in the DG equal the number of sensors in the geometry. As the correlation increases $\alpha \to 1$, then $\sum_\gamma 1^{|\gamma|}\kappa[\gamma] = \mathcal{I}^2$, and both DGs converge to 1 indicating no noise suppression is achieved at the output.

C. Detection Gain for the CSA_{pp}

More care is required to derive the CSA_{pp} DG since this processor is nonlinear, so (4) is explicitly used. Substituting $\mathcal{I}_M\mathcal{I}_N$ and $\kappa_{csa}^{pp}[\gamma]$ into (6), the CSA_{pp} output noise power is

$$E\{\text{ONP}_{csa}^{pp}(\alpha)\} = \sigma_W^2 \frac{1}{\mathcal{I}_M\mathcal{I}_N} \sum\nolimits_\gamma \alpha^{|\gamma|}\kappa_{csa}^{pp}[\gamma]. \tag{9}$$

The second moment of the noise power estimate $E\{(\check{y}_{csa}^{pp})^2|H_0\}$ is required to find the CSA_{pp} null hypothesis output variance. Results from [46], [47] on the fourth order moment of complex Gaussian random variables eventually leads to

$$E\{(\text{ONP}_{csa}^{pp}(\alpha))\,(\text{ONP}_{csa}^{pp}(\alpha))^*\} = \sigma_W^4 \frac{1}{(\mathcal{I}_M\mathcal{I}_N)^2} \sum(\alpha) \tag{10}$$

where

$$\sum(\alpha) = \sum_{a=0}^{\mathcal{I}_M-1} \sum_{b=0}^{\mathcal{I}_N-1} \sum_{d=0}^{\mathcal{I}_M-1} \sum_{e=0}^{\mathcal{I}_N-1} \left(\alpha^{|aM-bN|+|dM-eN|} + \alpha^{|aM-dM|+|bN-eN|}\right) \tag{11}$$

The complete derivation of the covariance to find $\sum(\alpha)$ is shown in the Appendix, and numerical simulations confirm the accuracy of the expression below. After substitution, the CSA_{pp} DG as a function of the spatial correlation $0 \le \alpha < 1$ reduces to

$$\sqrt{\mathcal{I}_M\mathcal{I}_N} \ge \frac{\mathcal{I}_M\mathcal{I}_N}{\sqrt{\sum(\alpha) - \left(\sum_\gamma \alpha^{|\gamma|}\kappa_{csa}^{pp}[\gamma]\right)^2}} > 1. \tag{12}$$

For white noise, the CSA_{pp} DG reduces to $\text{DG}_{csa}^{pp}(0) = \sqrt{\mathcal{I}_M\mathcal{I}_N}$, the geometric mean of the number of sensors in each subarray. Similar to the other processors, the CSA_{pp} DG also converges to 1 as $\alpha \to 1$.

D. Detection Gain Simulation Results

Fig. 3 shows the analytical (solid line) and simulated (· marker· line) DGs for 15000 Monte-Carlo trials. The horizontal is plotted on $\log_{10}(1-\alpha)$ scale to better depict the DG behavior around $0.9 \le \alpha < 1$ in the top panel, with a smaller range of $0 \le \alpha < 0.7$ in the bottom panel.

To make a commensurate comparison, the CSA processors' detection performances are first compared to the baseline of an unaliased ULA with the same number of sensors so both geometries have the same amount of available data, with $\mathcal{I}_{csa} = L = 100$. The CSA is composed of subarrays undersampled by $M = 5$, $N = 6$, extended by $P = 10$ periods. The aperture achieved by this sparse geometry ($\approx 150\lambda_o$) is about three times the filled ULA ($\approx 50\lambda_o$). This results in greater resolution for the CSA for estimating the spatial spectrum, but this paper focuses on the detection performance of CSAs.

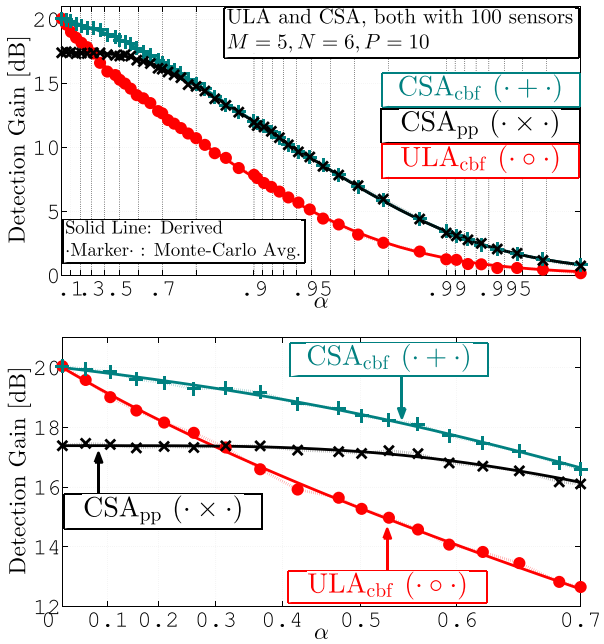

Fig. 3. Plot of DG versus increasing α for $u_s = 0$. A CSA composed of subarrays undersampled by $M = 5$, $N = 6$, extended by $P = 10$ periods, for a total of $\mathcal{I}_{csa} = 100$ sensors is compared to a ULA of $L = 100$ sensors. (top) $0 \leq \alpha < 1$ (bottom) $0 \leq \alpha < 0.7$. The CSA_{pp} initially has the lowest white noise gain of 17.4 dB, but the black CSA_{pp} curve does remain flatter than the teal CSA_{cbf} and red ULA_{cbf} curves as correlation increases from $0 < \alpha < 0.4$, indicating the CSA_{pp} is more robust to increasing noise correlation than the CSA_{cbf} or ULA_{cbf}.

The CSA_{cbf} and the ULA_{cbf} have white noise DGs equal to the number of sensors of 20 dB at the asymptote of $\alpha = 0$; the CSA_{pp} has the lowest white noise DG of 17.4 dB. As correlation increases, the teal CSA_{cbf} curve maintains the highest DG whereas the red ULA_{cbf} curve has the fastest rate of decay. Meanwhile, the black CSA_{pp} curve remains flatter than the other curves as correlation increases from $\alpha > 0$, indicating the CSA_{pp} is more robust to increasing correlation than the CSA_{cbf} or the ULA_{cbf}. The CSA_{pp} maintains the same DG for $\alpha < 0.4$, and already has greater DG than the ULA for $\alpha > 0.3$. For correlation beyond $\alpha = 0.8$, the two CSA DGs are essentially the same. As the noise approaches perfect coherence $\alpha \to 1$, all the DGs converge to 0 dB as predicted previously, rendering all arrays and algorithms useless.

Fig. 4 shows a plot of the same ULA with 100 sensors compared to a CSA with similar aperture, composed of subarrays undersampled by $M = 2$, $N = 5$, extended by $P = 10$ periods for a total of $\mathcal{I}_{csa} = 60$ sensors. The CSA_{cbf} has a white noise gain of the number of sensors 17.8 dB. The CSA_{pp} has a white noise gain of 15 dB, which is the geometric mean of the individual subarray DGs. Because the CSA has fewer sensors than the ULA of similar aperture, neither CSA processor DGs go above the ULA curve. However, all array processor DGs are essentially the same for $\alpha > 0.8$.

As the noise becomes correlated, the spatial noise energy compresses towards broadside in the signal direction [45], [48], degrading the beamformer detection performances. The CSA detection gain being greater than the sensor-constrained ULA

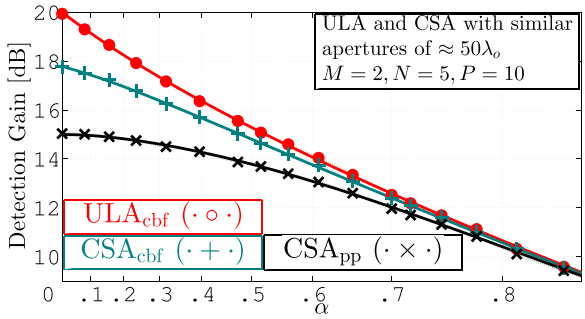

Fig. 4. Plot of DG for a CSA composed of subarrays undersampled by $M = 2$, $N = 5$, extended by $P = 10$ periods, for a total of $\mathcal{I}_{csa} = 60$ sensors versus a ULA with similar aperture of $L = 100$ sensors. The DG for the CSA with fewer sensors and comparable aperture never exceeds the red ULA curve, but they are essentially the same for $\alpha > 0.8$.

could be due partly to the CSA aperture being much greater than the ULA aperture. This implies greater spatial resolution to better discriminate targets as well as rejecting more noise within the main beam. It is fair to ask how the CSA processors' *estimation* performances compare to each other and the ULA_{cbf} of similar aperture as the noise correlation increases. This question is addressed in [45], [48], and the estimation results for the CSA presented there further illustrate the CSA_{pp} robustness against correlated noise compared to its CBF counterpart.

IV. Detection Performance

The test statistic, modeled by the random variable Z, transforms the input Gaussians at the CBF outputs based on the energy detector definition for the different algorithms.

The complimentary cumulative distribution function (CCDF) evaluated at a detection threshold τ under hypothesis $i \in \{0, 1\}$ gives the probability of false alarm and detection, respectively, to evaluate the ROC [21],

$$\mathcal{P}_i(\tau) = \Pr[Z > \tau | H_i] = \int_{\tau}^{\infty} f_{Z|H_i}(z|H_i) dz. \tag{13}$$

A. ULA_{cbf} and CSA_{cbf} Probability Distribution Functions

The test statistic for the ULA_{cbf} and CSA_{cbf} energy detector is the magnitude of the CBF output power, defined as $Z = |\check{Y}| = |Y^2|$. The input Gaussian distribution Y transforms to a central χ^2-distribution with two degrees of freedom [49],

$$f_{Z|H_i}(z, \alpha) = \frac{1}{2\sigma_i^2(\alpha)} \exp\left(-\frac{z}{2\sigma_i^2(\alpha)}\right), z \geq 0 \tag{14}$$

where $\sigma_i^2(\alpha)$ is the variance at the beamformer output under the hypothesis $i \in \{0, 1\}$, and $\sigma_0^2(\alpha) = (\sigma_W^2 / \mathcal{I}^2) \sum_\gamma \alpha^{|\gamma|} \kappa[\gamma]$ from (6), and $\sigma_1^2(\alpha) = \sigma_S^2 + \sigma_0^2(\alpha)$.

The CCDF for the CBF energy detector as a function of α is given by the exponential function [49],

$$\mathcal{P}_i(\tau, \alpha) = \exp\left(-\frac{\tau}{2\sigma_i^2(\alpha)}\right), i \in \{0, 1\}. \tag{15}$$

B. CSA_{pp} Probability Distribution Function

The CSA_{pp} output is defined as $\check{y}_{csa}^{pp} = y_M y_N^*$ [1], which is already in units of power. The CSA_{pp} energy detector is modeled as $Z_{csa}^{pp} = |\check{Y}_{csa}^{pp}| = |Y_M Y_N^*| = |Y_M||Y_N|$. The magnitude of the CBF subarray output transforms the input Gaussian into a Rayleigh distribution. The subarrays share sensors, which inherently makes the subarray outputs correlated, even for the case of spatially white noise. The CSA_{pp} output PDF is therefore characterized by the product of two dependent Rayleigh random variables [14], [49],

$$f_Z(z,\alpha) = \frac{z}{\sigma_M^2\sigma_N^2(1-\rho^2)} I_0\left(\frac{z|\rho|}{\sigma_M\sigma_N(1-\rho^2)}\right) \times K_0\left(\frac{z}{\sigma_M\sigma_N(1-\rho^2)}\right), z \geq 0 \tag{16}$$

where the dependence of σ_M, σ_N, and ρ on α has been suppressed for brevity. The modified Bessel functions I_0 and K_0 are of the first and second kind respectively. Asymptotic expansions of I_0 and K_0 show for large arguments [50], the CSA_{pp} PDF approaches an exponential distribution,[‡]

$$f_Z(z,\alpha) \approx \frac{1}{\sigma^2_{csa_{pp}}(\alpha)} \exp\left(-\frac{z}{\sigma^2_{csa_{pp}}(\alpha)}\right). \tag{17}$$

The rate parameter for the asymptotic expansion is defined as

$$\sigma^2_{csa_{pp}}(\alpha) = \frac{\sigma_M\sigma_N(1-\rho^2)}{(1-|\rho|)} \tag{18}$$

where σ_M^2 and σ_N^2 are the CBF subarray variances, found for one subarray using (6) for the noise only case. The correlation coefficient between the subarray outputs is $\rho \triangleq E\{Y_M Y_N^*\}/\sqrt{\sigma_M^2\sigma_N^2}$. After substitution, the alternate hypothesis correlation coefficient is

$$\rho_1(\alpha) = \left(\frac{\sigma_S^2}{\sigma_W^2} + \frac{1}{\mathcal{I}_M\mathcal{I}_N}\sum\nolimits_\gamma \alpha^{|\gamma|}\kappa_{csa}^{pp}[\gamma]\right) \times \left(\frac{\sigma_S^2}{\sigma_W^2} + \frac{1}{\mathcal{I}_M^2}\sum\nolimits_\gamma \alpha^{|\gamma|}\kappa_M[\gamma]\right)^{-1/2} \times \left(\frac{\sigma_S^2}{\sigma_W^2} + \frac{1}{\mathcal{I}_N^2}\sum\nolimits_\gamma \alpha^{|\gamma|}\kappa_N[\gamma]\right)^{-1/2}. \tag{19}$$

Adhikari and Buck assert the noise only correlation coefficient is negligible for large coprime factors $M, N > 4$ [14]. For white noise as the only input, the correlation coefficient reduces to $\rho_0(0) = 1/\sqrt{MN}$. At the other asymptote, as $\alpha \to 1$, the noise becomes highly correlated, and the correlation coefficient $\rho \to 1$ as expected. For spatially correlated noise between these extremes, increasing the undersampling factors M, N increases the intersensor spacing, and thus also increases the spacing between the shared sensors. For a given value of α, increasing the spacing between shared sensors decreases ρ, indicating that the subarray outputs grow less correlated.

[‡]The exponential approximation in (17) is used when (16) fails in MATLAB due to large arguments in the Bessel functions. Such cases occur when ρ approaches 1, or when any of the CSA parameters M, N, P approach infinity since σ_M or σ_N will approach 0 under the null hypothesis. Kolmogorov-Smirnov tests were performed and verified the predicted PDF against the numerical simulations [45], [51].

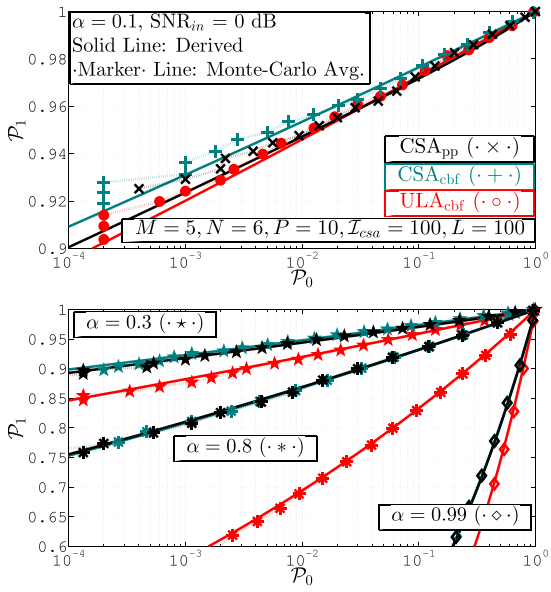

Fig. 5. (Top) ROCs for $\alpha = 0.1$ and $\mathrm{SNR}_{in} = 0$ dB. The $\mathrm{CSA_{cbf}}$ ROC is closest to the upper left corner of the ROC, indicating the best detection performance. Meanwhile, the $\mathrm{CSA_{pp}}$ and $\mathrm{ULA_{cbf}}$ ROCs lie on top of one another, and closely match the $\mathrm{CSA_{cbf}}$, indicating the deflection statistic under-predicts the $\mathrm{CSA_{pp}}$ performance. (Bottom) ROCs for $\alpha = 0.3(\cdot\star\cdot)$, $\alpha = 0.8(\cdot*\cdot)$, $\alpha = 0.99(\cdot\diamond\cdot)$. The ROCs illustrate the performances degrade as inter-sensor correlation increases in a similar fashion to what the deflection depicted in Fig. 3.

C. ROC Performance Simulation Results

The ROCs shown in Fig. 5 consider the sensor constrained array geometries and simulation parameters as in Section III. The top panel shows a single case of ROCs to begin the discussion on the relationship between the ROC and deflection statistic performances. The bottom panel provides a few more ROCs as the correlation increases to further the discussion.

The top panel shows the three processors' ROCs for $\alpha = 0.1$ and $\mathrm{SNR}_{in} = 0$ dB. The $\mathrm{CSA_{cbf}}$ has the highest ROC, though the $\mathrm{CSA_{pp}}$ ROC is a close match. This suggests the deflection statistic under-predicts the $\mathrm{CSA_{pp}}$ performance, since $\mathrm{DG}_{csa}^{cbf}(0.1) > \mathrm{DG}_{csa}^{pp}(0.1)$ (see Fig. 3). Comparing the $\mathrm{CSA_{pp}}$ with the $\mathrm{ULA_{cbf}}$ performances, the deflection predicts $\mathrm{DG}_{ula}(0.1) > \mathrm{DG}_{csa}^{pp}(0.1)$, but their ROCs are virtually the same. Although the deflection eventually predicts $\mathrm{DG}_{csa}^{pp} > \mathrm{DG}_{ula}$ for $\alpha > 0.3$ and $\mathrm{DG}_{csa}^{pp} = \mathrm{DG}_{csa}^{cbf}$ for $\alpha > 0.8$, the ROCs show the $\mathrm{CSA_{cbf}}$ and ULA detection performances degrade much sooner relative to the $\mathrm{CSA_{pp}}$ as inter-sensor correlation increases. The ROCs

further support the robustness of CSA_{pp} to increasing correlation in background noise.

The bottom panel of Fig. 5 shows the ROCs for increasing values of α. For $\alpha = 0.3$, where the deflection predicts $\text{DG}_{csa}^{cbf}(0.3) > \{\text{DG}_{csa}^{pp}(0.3) = \text{DG}_{ula}(0.3)\}$, the plot shows again the CSA_{pp} ROC closely matches the CSA_{cbf}, and is greater than the ULA_{cbf} ROC. As correlation increased to $\alpha = 0.8$, the separation between the two CSA ROCs and the ULA_{cbf} ROC become much greater. As $\alpha \to 1$, the ROCs begin to approach the same sensitivities. The behavior of the latter two cases of α was to be expected given the deflection results.

V. Discussion and Conclusion

Adhikari and Buck derived the conditional PDFs and ROCs for the CSA_{pp} output energy detector for spatially white background noise [14]. They approximated the product of the Bessel functions at the large argument asymptote to be exponentially distributed, like the ULA energy detector PDF. They also compared the CSA_{pp} ROC performances with ULAs of comparable aperture, and found that by increasing the CSA's input SNR relative to the ULA's input SNR by the ratio of the number of sensors in the respective geometries, the CSA_{pp} ROC matched the ULA's ROC. These analytical approximations combined with the simulations confirmed that the CSA_{pp} DG in white noise is also proportional to the number of sensors in its geometry despite the nonlinear processing.

This paper derived the DGs, conditional PDFs, and ROCs for the CSA and ULA for spatially correlated background noise. The study shown here made a more commensurate comparison of the CSA_{pp} detection performance than [14] by comparing the CSA_{pp} against its CBF counterpart and the ULA_{cbf} composed of the same number of sensors, with both geometries experiencing the same input SNR. The CSA_{pp} ROCs closely matched the CSA_{cbf} even for $\alpha = 0.1$, and outperformed the sensor-constrained ULA_{cbf} when the inter-sensor noise correlation increases. Despite the deflection statistic predicting that the detection performance of CSA_{pp} is lower than that of the CSA_{cbf}, the conditional PDFs and ROCs derived here support the previous conclusion by [14] that the DG of the CSA_{pp} is proportional to the number of sensors in the geometry.

As shown, the deflection does not perfectly predict the CSA_{pp} ROC performance. While the deflection statistic is simpler to estimate because it only requires the moments of the conditional PDFs, this single scalar only provides a coarse view of the relative performance of different detectors as a function of the spatial correlation of the noise [24]. The deflection does not completely characterize detection performance when the conditional PDFs have different functional forms, and thus different shapes to the PDF's tails. Measuring the relative separation of the means of the conditional PDFs does not fully characterize the detection performance which does depend on the tails of the distribution. At a more detailed level, the ROCs take into account the *shape* of the conditional PDFs via the CCDF, and provide a more complete characterization of detection performance [45]. However, the deflection still remains a more useful prediction of relative performance of nonlinear detectors than the classic array gain ratio of output to input SNR.

In conclusion, this paper analyzes the detection performance for Gaussian signals in spatially white noise for the CSA_{pp} detector, and compares this performance to both the CSA_{cbf} and ULA_{cbf} detectors. At a basic level, the deflection statistics were derived to quantify the DGs. These DGs were shown to depend on the coarray function and the number of sensors in the "subarrays" embedded in the array processor. The deflection statistic indicates that although the CSA_{pp} has less DG than the other two detectors, the product processor is relatively speaking more robust to increasing spatial correlation in the noise than the other detectors. Deriving the conditional PDFs to evaluate the ROCs provided a more complete understanding of the detection performance as a function of noise correlation. The ROC curves demonstrated that as the inter-sensor correlation increases, the CSA_{cbf} and ULA detection performances degrade relative to the CSA_{pp} much sooner than predicted by the deflection.

Appendix

This appendix derives the second moment of the noise power estimate $E\left\{(\breve{y}_{csa}^{pp})^2|H_0\right\}$ used in the deflection by calculating the CSA_{pp} cross-spectral density.

$$E\left\{\text{ONP}_{csa}^{pp}(u_1)\cdot\text{ONP}_{csa}^{pp}(u_2)^*\right\} = \frac{1}{(\mathcal{I}_M\mathcal{I}_N)^2} \times E\left\{\sum_{a=0}^{\mathcal{I}_M-1}\sum_{b=0}^{\mathcal{I}_N-1} c[aM]c^*[bN]\exp(-j\pi[aM-bN]u_1) \times \sum_{d=0}^{\mathcal{I}_M-1}\sum_{e=0}^{\mathcal{I}_N-1} c^*[dM]c[eN]\exp(j\pi[dM-eN]u_2)\right\} \quad (20)$$

After moving the expectation into the sums and substituting in for the noise model,

$$E\left\{\text{ONP}_{csa}^{pp}(u_1)\cdot\text{ONP}_{csa}^{pp}(u_2)^*\right\} = (1-\alpha^2)^2\frac{1}{(\mathcal{I}_M\mathcal{I}_N)^2} \times \sum_{a=0}^{\mathcal{I}_M-1}\sum_{b=0}^{\mathcal{I}_N-1}\exp(-j\pi[aM-bN]u_1) \times \sum_{d=0}^{\mathcal{I}_M-1}\sum_{e=0}^{\mathcal{I}_N-1}\exp(j\pi[dM-eN]u_2) \times E\left\{\sum_{h=0}^{\infty}\alpha^h n[aM-h]\sum_{i=0}^{\infty}\alpha^i n^*[bN-i] \times \sum_{j=0}^{\infty}\alpha^j n^*[dM-j]\sum_{k=0}^{\infty}\alpha^k n[eN-k]\right\} \quad (21)$$

The expectation on the RHS of (21) can again be moved inside all of the sums over α,

$$E\{\cdot\} = \sum_{h=0}^{\infty}\sum_{i=0}^{\infty}\sum_{j=0}^{\infty}\sum_{k=0}^{\infty}\alpha^{h+i+j+k} \times E\{n[aM-h]n^*[bN-i]n^*[dM-j]n[eN-k]\} \tag{22}$$

For a complex Gaussian noise process with power σ_W^2, the expected value $E\left\{n[\bar{a}]n^*[\bar{b}]n^*[\bar{d}]n[\bar{e}]\right\}$ becomes [46],

$$E\{n[aM-h]n^*[bN-i]\}E\{n^*[dM-j]n[eN-k]\} + E\{n[aM-h]n^*[dM-j]\}E\{n^*[bN-i]n[eN-k]\} \tag{23}$$

Note for the first term of the sum from (23),

$$E\{n[aM-h]n^*[bN-i]\}\,E\{n^*[dM-h]n[eN-i]\} = \begin{cases}\sigma_W^4 \text{ for } aM-h=bN-i \cap dM-j=eN-k \\ 0 \text{ otherwise}\end{cases} = \begin{cases}\sigma_W^4 \text{ for } aM-bN=h-i \cap dM-eN=j-k \\ 0 \text{ otherwise}\end{cases}$$

Similarly for the second term of the sum from (23),

$$E\{n[aM-h]n^*[dM-j]\}\,E\{n^*[bN-i]n[eN-k]\} = \begin{cases}\sigma_W^4 \text{ for } aM-h=dM-j \cap bN-i=eN-k \\ 0 \text{ otherwise}\end{cases} = \begin{cases}\sigma_W^4 \text{ for } aM-dM=h-j \cap bN-eN=i-k \\ 0 \text{ otherwise}\end{cases}$$

It will be convenient to define a new lag term variable γ for each set within the two terms, with $aM-bN=h-i=\gamma_c$, and $dM-eN=j-k=\gamma_f$ for the first term of (23), and $aM-dM=h-j=\gamma_m$, and $bN-eN=i-k=\gamma_n$ for the second term. It will first be helpful to rearrange the sums over α and group them accordingly,

$$\sigma_W^4 \underbrace{\sum_{h=0}^{\infty}\sum_{i=0}^{\infty}\alpha^{h+i}}_{\text{Group 1}}\underbrace{\sum_{j=0}^{\infty}\sum_{k=0}^{\infty}\alpha^{j+k}}_{\text{Group 2}} + \sigma_W^4 \underbrace{\sum_{h=0}^{\infty}\sum_{j=0}^{\infty}\alpha^{h+j}}_{\text{Group 3}}\underbrace{\sum_{i=0}^{\infty}\sum_{k=0}^{\infty}\alpha^{i+k}}_{\text{Group 4}}$$

The following loop iterations assumes the simplest CSA sampling geometry composed of subarrays undersampled by $M=2$, $N=3$, extended by $P=1$ periods to illuminate the ultimate pattern. The first loop iteration with $a=0,b=0,d=0,e=0$ reduces the grouped sums easily since $i=h-0$ for Group 1, $j=k-0$ for Group 2, etc., allowing the sums to be combined,

$a=0,b=0,d=0,e=0 \rightarrow$

First term: $\gamma_c=0 \cap \gamma_f=0 \rightarrow$

$$\sigma_W^4 \underbrace{\sum_{h=0}^{\infty}\alpha^{2h-0}}_{\text{Group 1 combined}} \cdot \underbrace{\sum_{j=0}^{\infty}\alpha^{2j-0}}_{\text{Group 2 combined}} = \sigma_W^4\frac{\alpha^0}{(1-\alpha^2)^2}$$

$+$

Second term: $\gamma_m=0 \cap \gamma_n=0 \rightarrow$

$$\sigma_W^4 \underbrace{\sum_{h=0}^{\infty}\alpha^{2h-0}}_{\text{Group 3 combined}} \cdot \underbrace{\sum_{i=0}^{\infty}\alpha^{2i-0}}_{\text{Group 4 combined}} = \sigma_W^4\frac{\alpha^0}{(1-\alpha^2)^2}$$

The next loop iteration covered will be $a=0,b=0,d=1,e=0$, with subsequent lag terms being $\gamma_c=0$, $\gamma_f=2$, $\gamma_m=-2$, and $\gamma_n=0$. It is easy to see that the Group 1 sum will be $\sum_{h=0}^{\infty}\alpha^{2h-0}$ after substituting $i=h-0$. For the Group 2 sum (as well as any other Group sum), it is important to note h,i,j,k all must start at 0 or greater. The substitution of $k=j-2$ reduces Group 2 to $\sum_{j=2}^{\infty}\alpha^{2j-2}$. The product of Groups 1 and 2 is

$$\sigma_W^4 \underbrace{\sum_{h=0}^{\infty}\alpha^{2h-0}}_{\text{Group 1 combined}} \cdot \underbrace{\sum_{j=2}^{\infty}\alpha^{2j-2}}_{\text{Group 2 combined}} = \sigma_W^4\frac{\alpha^2}{(1-\alpha^2)^2}$$

The second term reduces similarly; after substituting $h=j-2$, the Group 3 sum reduces to $\sum_{j=2}^{\infty}\alpha^{2j-2}$. The Group 4 sum, after substituting $k=i-0$ reduces to $\sum_{i=0}^{\infty}\alpha^{2i-0}$. The product of Groups 3 and 4 is

$$\sigma_W^4 \underbrace{\sum_{j=2}^{\infty}\alpha^{2j-2}}_{\text{Group 3 combined}} \cdot \underbrace{\sum_{i=0}^{\infty}\alpha^{2i-0}}_{\text{Group 4 combined}} = \sigma_W^4\frac{\alpha^2}{(1-\alpha^2)^2}$$

This iteration showed with either positive or negative γ lag terms, the sums must be rearranged such that the resulting power term of α for the product of Groups 1 and 2 is $|\gamma_c|+|\gamma_f|$. Similarly, the resulting power term of α for Groups 3 and 4 is $|\gamma_m|+|\gamma_n|$. The following select iterations are shown for completeness.

$a=0,b=1,d=0,e=0 \rightarrow$

First term: $\gamma_c=-3 \cap \gamma_f=0 \rightarrow$

$$\sigma_W^4 \underbrace{\sum_{i=3}^{\infty}\alpha^{2i-3}}_{\text{Group 1 combined}} \cdot \underbrace{\sum_{j=0}^{\infty}\alpha^{2j-0}}_{\text{Group 2 combined}} = \sigma_W^4\frac{\alpha^3}{(1-\alpha^2)^2}$$

$+$

Second term : $\gamma_m=0 \cap \gamma_n=3 \rightarrow$

$$\sigma_W^4 \underbrace{\sum_{h=0}^{\infty}\alpha^{2h-0}}_{\text{Group 3 combined}} \cdot \underbrace{\sum_{i=3}^{\infty}\alpha^{2i-3}}_{\text{Group 4 combined}} = \sigma_W^4\frac{\alpha^3}{(1-\alpha^2)^2}$$

$a=1,b=1,d=0,e=0 \rightarrow$

First term: $\gamma_c=-1 \cap \gamma_f=0 \rightarrow$

$$\sigma_W^4 \underbrace{\sum_{i=1}^{\infty}\alpha^{2i-1}}_{\text{Group 1 combined}} \cdot \underbrace{\sum_{j=0}^{\infty}\alpha^{2j-0}}_{\text{Group 2 combined}} = \sigma_W^4 \frac{\alpha^1}{(1-\alpha^2)^2}$$

$+$

Second term: $\gamma_m=2 \cap \gamma_n=3 \rightarrow$

$$\sigma_W^4 \underbrace{\sum_{h=2}^{\infty}\alpha^{2h-2}}_{\text{Group 3 combined}} \cdot \underbrace{\sum_{i=3}^{\infty}\alpha^{2i-3}}_{\text{Group 4 combined}} = \sigma_W^4 \frac{\alpha^5}{(1-\alpha^2)^2}$$

$a=1,b=0,d=1,e=0 \rightarrow$

First term: $\gamma_c=2 \cap \gamma_f=2 \rightarrow$

$$\sigma_W^4 \underbrace{\sum_{h=2}^{\infty}\alpha^{2h-2}}_{\text{Group 1 combined}} \cdot \underbrace{\sum_{j=2}^{\infty}\alpha^{2j-2}}_{\text{Group 2 combined}} = \sigma_W^4 \frac{\alpha^4}{(1-\alpha^2)^2}$$

$+$

Second term: $\gamma_m=0 \cap \gamma_n=0 \rightarrow$

$$\sigma_W^4 \underbrace{\sum_{h=0}^{\infty}\alpha^{2h-0}}_{\text{Group 3 combined}} \cdot \underbrace{\sum_{i=0}^{\infty}\alpha^{2i-0}}_{\text{Group 4 combined}} = \sigma_W^4 \frac{\alpha^0}{(1-\alpha^2)^2}$$

$a=1,b=0,d=0,e=1 \rightarrow$

First term: $\gamma_c=2 \cap \gamma_f=-3 \rightarrow$

$$\sigma_W^4 \underbrace{\sum_{h=2}^{\infty}\alpha^{2h-2}}_{\text{Group 1 combined}} \cdot \underbrace{\sum_{k=3}^{\infty}\alpha^{2k-3}}_{\text{Group 2 combined}} = \sigma_W^4 \frac{\alpha^5}{(1-\alpha^2)^2}$$

$+$

Second term: $\gamma_m=2 \cap \gamma_n=-3 \rightarrow$

$$\sigma_W^4 \underbrace{\sum_{h=2}^{\infty}\alpha^{2h-2}}_{\text{Group 3 combined}} \cdot \underbrace{\sum_{k=3}^{\infty}\alpha^{2k-3}}_{\text{Group 4 combined}} = \sigma_W^4 \frac{\alpha^5}{(1-\alpha^2)^2}$$

$a=2,b=1,d=0,e=0 \rightarrow$

First term: $\gamma_c=1 \cap \gamma_f=2 \rightarrow$

$$\sigma_W^4 \underbrace{\sum_{h=1}^{\infty}\alpha^{2h-1}}_{\text{Group 1 combined}} \cdot \underbrace{\sum_{j=2}^{\infty}\alpha^{2j-2}}_{\text{Group 2 combined}} = \sigma_W^4 \frac{\alpha^3}{(1-\alpha^2)^2}$$

$+$

Second term: $\gamma_m=2 \cap \gamma_n=-3 \rightarrow$

$$\sigma_W^4 \underbrace{\sum_{h=2}^{\infty}\alpha^{2h-2}}_{\text{Group 3 combined}} \cdot \underbrace{\sum_{i=3}^{\infty}\alpha^{2i-3}}_{\text{Group 4 combined}} = \sigma_W^4 \frac{\alpha^5}{(1-\alpha^2)^2}$$

$a=2,b=1,d=1,e=1 \rightarrow$

First term: $\gamma_c=1 \cap \gamma_f=-1 \rightarrow$

$$\sigma_W^4 \underbrace{\sum_{h=1}^{\infty}\alpha^{2h-1}}_{\text{Group 1 combined}} \cdot \underbrace{\sum_{k=1}^{\infty}\alpha^{2k-1}}_{\text{Group 2 combined}} = \sigma_W^4 \frac{\alpha^2}{(1-\alpha^2)^2}$$

$+$

Second term: $\gamma_m=2 \cap \gamma_n=0 \rightarrow$

$$\sigma_W^4 \underbrace{\sum_{h=2}^{\infty}\alpha^{2h-2}}_{\text{Group 3 combined}} \cdot \underbrace{\sum_{i=0}^{\infty}\alpha^{2i-0}}_{\text{Group 4 combined}} = \sigma_W^4 \frac{\alpha^2}{(1-\alpha^2)^2}$$

The resulting pattern simplifies the expectation from (21) to the four sums that originally indexed over the sensor indices,

$$\begin{aligned} &E\left\{\text{ONP}_{csa}^{pp}(u_1)\cdot \text{ONP}_{csa}^{pp}(u_2)^*\right\} \\ &\quad= \sigma_W^4 \frac{1}{(\mathcal{I}_M\mathcal{I}_N)^2}\sum_{a=0}^{\mathcal{I}_M-1}\sum_{b=0}^{\mathcal{I}_N-1}\sum_{d=0}^{\mathcal{I}_M-1}\sum_{e=0}^{\mathcal{I}_N-1} \\ &\qquad\times \exp(-j\pi(u_1[aM-bN]+u_2[dM-eN])) \\ &\qquad\times \left(\alpha^{|aM-bN|+|dM-eN|}+\alpha^{|aM-dM|+|bN-eN|}\right) \end{aligned}$$

The exponential will be rearranged with $\Delta u=u_1-u_2$ such that the covariance for a particular direction can be calculated by setting $\Delta u=0$,

$$\begin{aligned} &\exp(-j\pi(u_1[aM-bN]+u_2[dM-eN])) \\ &\quad=\exp(-j\pi\Delta u([aM-bN]+[dM-eN]) \\ &\qquad\times\exp(-j\pi(u_1[dM-eN]-u_2[aM-bN]) \end{aligned}$$

Although the noise is assumed to be WSS, the colored noise auto-correlation function is truncated, which breaks the WSS assumption when calculating the cross-covariance. Hence, the cross-covariance is dependent on both look directions u_1 and u_2 when the noise is spatially correlated, in contrast to being dependent only on the difference Δu.

The cross-covariance calculation will be broken into two terms,

$$\begin{aligned} &E\left\{\text{ONP}_{csa}^{pp}(u_1)\cdot \text{ONP}_{csa}^{pp}(u_2)^*\right\} \\ &\qquad\times\sigma_W^4\frac{1}{(\mathcal{I}_M\mathcal{I}_N)^2}\sum(\alpha,u_1,u_2) \end{aligned}$$

where $\sum(\alpha,u_1,u_2)=A+B$,

$$\begin{aligned} A(\alpha,u_1,u_2)=&\sum_{a,b,d,e}\alpha^{|aM-bN|+|dM-eN|} \\ &\times\exp(-j\pi\Delta u([aM-bN]+[dM-eN])) \\ &\times\exp(-j\pi(u_2[aM-bN]-u_1[dM-eN])) \end{aligned}$$

and

$$B(\alpha, u_1, u_2) \sum_{a,b,d,e} \alpha^{|aM-dM|+|bN-eN|} \times \exp(-j\pi\Delta u([aM-bN]+[dM-eN])) \times \exp(-j\pi(u_2[aM-bN]-u_1[dM-eN]))$$

CSA$_{\text{pp}}$ Covariance

When the noise is spatially white, the fourth order expectation simplifies to

$$E\{n[aM]n^*[bN]n^*[dM]n[eN]\} = \sigma^4(\delta[aM-bN]\delta[dM-eN]+\delta[aM-dM]\delta[bN-eN])$$

The A term is scaled by $\sigma^4(\delta[aM-bN]\delta[dM-eN])$, and the B term is scaled by $\sigma^4(\delta[aM-dM]\delta[bN-eN])$.

For the A term, the expectation is non-zero only at the shared sensors, i.e., $aM = bN$, and similarly $dM = eN$. Both the exponential and α terms all go to 1, and the four summations result in a factor of $A(0,\Delta u) = P^2$.

For the B term, the impulses indicate the expectation will be non-zero for $aM = dM$, and $bN = eN$. For the special case of spatially white noise, the covariance will be dependent only on Δu. Once again, this will cause the α term to simplify to 1, while the exponential reduces to,

$$B(0,\Delta u) = \sum_{a=0}^{\mathcal{I}_M-1}\sum_{b=0}^{\mathcal{I}_N-1} \exp(-j\pi[aM-bN]\Delta u) = \sum_{a=0}^{\mathcal{I}_M-1}\exp(-j\pi aM\Delta u)\sum_{b=0}^{\mathcal{I}_N-1}\exp(j\pi bN\Delta u)$$

Using the formula for finite geometric sums, and then factoring out half of the exponential terms in both the numerators and denominators, the two sums reduce to a product of sinc functions,

$$B(0,\Delta u) = \frac{\exp(-j\pi\frac{N-M}{2}\Delta u)\sin^2(\frac{\pi}{2}MNP\Delta u)}{\sin(\frac{\pi}{2}M\Delta u)\sin(\frac{\pi}{2}N\Delta u)}$$

Subtracting the square of the mean for the white noise case ($\sum_\gamma 0^{|\gamma|}\kappa_{csa}^{pp}[\gamma] = P)^2$ cancels out the A term, which reduces the covariance for the CSA$_{\text{pp}}$ in spatially white noise to

$$\text{Cov}(0,\Delta u) = \sigma_W^4\frac{1}{(\mathcal{I}_M\mathcal{I}_N)^2}\frac{\exp\left(-j\pi\frac{N-M}{2}\Delta u\right)\sin^2\left(\frac{\pi}{2}MNP\Delta u\right)}{\sin(\frac{\pi}{2}M\Delta u)\sin\left(\frac{\pi}{2}N\Delta u\right)} \quad (24)$$

The phasor $\exp(-j\pi\frac{N-M}{2}\Delta u)$ is a result of defining the phase reference as the left most sensor for each subarray.

When the noise is correlated, the additional phasors in $\sum(\alpha, u_1, u_2)$ must be considered. After substitution and simplification of the covariance for the signal arriving from $u_1 = u_s = u_2$, the A and B terms simplify to

$$A(\alpha, u_s) = \sum_{a,b,d,e} \alpha^{|aM-bN|+|dM-eN|} \times \exp(-j\pi(u_s[aM-bN]-u_s[dM-eN]))$$

and

$$B(\alpha, u_s) = \sum_{a,b,d,e} \alpha^{|aM-dM|+|bN-eN|} \times \exp(-j\pi(u_s[aM-bN]-u_s[dM-eN]))$$

The gain for the CSA$_{\text{pp}}$ for a signal arriving from u_s is generalized as

$$\text{DG}_{csa}^{pp}(\alpha, u_s) = \frac{\mathcal{I}_M\mathcal{I}_N}{\sqrt{\sum(\alpha,u_s) - \left(\sum\alpha^{|\gamma|}\kappa_{csa}^{pp}[\gamma]e^{-j\pi\gamma u_s}\right)^2}}.$$

ACKNOWLEDGMENT

The authors would like to thank Prof. K. Wage and the anonymous reviewers for helpful feedback in revising this manuscript.

REFERENCES

[1] P. P. Vaidyanathan and P. Pal, "Sparse sensing with co-prime samplers and arrays," *IEEE Trans. Signal Process.*, vol. 59, no. 2, pp. 573–586, Feb. 2011.

[2] R. T. Hoctor and S. A. Kassam, "The unifying role of the coarray in aperture synthesis for coherent and incoherent imaging," *Proc. IEEE*, vol. 78, no. 4, pp. 735–752, Apr. 1990.

[3] H. L. Van Trees, *Optimum Array Processing: Part IV of Detection, Estimation, and Modulation Theory*. New York, NY, USA: Wiley, 2002.

[4] S. Qin, Y. D. Zhang, and M. G. Amin, "Generalized coprime array configurations for direction-of-arrival estimation," *IEEE Trans. Signal Process.*, vol. 63, no. 6, pp. 1377–1390, Mar. 2015.

[5] S. Qin, Y. D. Zhang, M. G. Amin, and F. Gini, "Frequency diverse coprime arrays with coprime frequency offsets for multitarget localization," *IEEE J. Sel. Topics Signal Process.*, vol. 11, no. 2, pp. 321–335, Mar. 2017.

[6] S. U. Pillai, Y. Bar-Ness, and F. Haber, "A new approach to array geometry for improved spatial spectrum estimation," *Proc. IEEE*, vol. 73, no. 10, pp. 1522–1524, Oct. 1985.

[7] S. Pillai and F. Haber, "Statistical analysis of a high resolution spatial spectrum estimator utilizing an augmented covariance matrix," *IEEE Trans. Acoust., Speech, Signal Process.*, vol. 35, no. 11, pp. 1517–1523, Nov. 1987.

[8] C. Liu and P. P. Vaidyanathan, "Remarks on the spatial smoothing step in coarray music," *IEEE Signal Process. Lett.*, vol. 22, no. 9, pp. 1438–1442, Sep. 2015.

[9] R. Schmidt, "Multiple emitter location and signal parameter estimation," *IEEE Trans. Antennas Propag.*, vol. 34, no. 3, pp. 276–280, Mar. 1986.

[10] D. Johnson and D. Dudgeon, *Array Signal Processing: Concepts and Techniques*. Upper Saddle River, NJ, USA: Prentice-Hall, 1993.

[11] A. Moffet, "Minimum-redundancy linear arrays," *IEEE Trans. Antennas Propag.*, vol. 16, no. 2, pp. 172–175, Mar. 1968.

[12] P. Pal and P. P. Vaidyanathan, "Coprime sampling and the MUSIC algorithm," in *Proc. Digital Signal Process. Signal Process. Educ. Meeting*, Jan. 2011, pp. 289–294.

[13] K. Adhikari, J. R. Buck, and K. E. Wage, "Extending coprime sensor arrays to achieve the peak side lobe height of a full uniform linear array," *EURASIP J. Advances Signal Process.*, vol. 2014, pp. 148–165, Sep. 2014.

[14] K. Adhikari and J. R. Buck, "Gaussian signal detection by coprime sensor arrays," in *Proc. IEEE Int. Conf. Acoust., Speech Signal Process.*, Apr. 2015, pp. 2379–2383.

[15] K. Adhikari and J. R. Buck, "Spatial spectral estimation with product processing of a pair of colinear arrays," *IEEE Trans. Signal Process.*, vol. 65, no. 9, pp. 2389–2401, May 2017.

[16] Y. Liu and J. R. Buck, "Detecting Gaussian signals in the presence of interferers using the coprime sensor arrays with the min processor," in *Proc. 49th Asilomar Conf. Signals, Syst. Comput.*, Nov. 2015, pp. 370–374.

[17] Y. Liu and J. R. Buck, "Gaussian source detection and spatial spectral estimation using a coprime sensor array with the min processor," *IEEE Trans. Signal Process.*, vol. 66, no. 1, pp. 186–199, Jan. 2018.

[18] G. Di Martino and A. Iodice, "Passive beamforming with coprime arrays," *IET Radar, Sonar Navigat.*, vol. 11, no. 6, pp. 964–971, 2017.

[19] B. Wang, Y. D. Zhang, and W. Wang, "Robust DOA estimation in the presence of miscalibrated sensors," *IEEE Signal Process. Lett.*, vol. 24, no. 7, pp. 1073–1077, Jul. 2017.
[20] M. Wang and A. Nehorai, "Coarrays, MUSIC, and the Cramer-Rao bound," *IEEE Trans. Signal Process.*, vol. 65, no. 4, pp. 933–946, Feb. 2017.
[21] H. L. Van Trees, *Detection, Estimation, and Modulation Theory Part I*. New York, NY, USA: Wiley, 2001.
[22] J. L. Lawson and G. E. Uhlenbeck, *Threshold Signals* (M.I.T. Radiation Laboratory Series). Lexington MA, USA: Boston Technical Publishers, 1964, ch. 7.3, pp. 161–165.
[23] H. Cox, "Line array performance when the signal coherence is spatially dependent," *J. Acoustical Soc. Amer.*, vol. 55, no. 2, pp. 453–453, 1973.
[24] B. Picinbono, "On deflection as a performance criterion in detection," *IEEE Trans. Aerosp. Electron. Syst.*, vol. 31, no. 3, pp. 1072–1081, Jul. 1995.
[25] S. A. Kassam, *Signal Detection in Non-Gaussian Noise*. New York, NY, USA: Springer, 2012.
[26] W. A. Gardner, "A unifying view of second-order measures of quality for signal classification," *IEEE Trans. Commun.*, vol. 28, no. 6, pp. 807–816, Jun. 1980.
[27] D. R. Morgan and T. M. Smith, "Coherence effects on the detection performance of quadratic array processors, with applications to large-array matched-field beamforming," *J. Acoustical Soc. Amer.*, vol. 87, no. 2, pp. 737–747, 1990.
[28] W. S. Burdic, *Underwater Acoustic Systems Analysis*. Englewood Cliffs, NJ, USA: Prentice-Hall, 1991.
[29] B. Steinberg, *Principles of Aperture and Array System Design: Including Random and Adaptive Arrays*. Canada, U.K.: Wiley, 1976.
[30] E. N. Gilbert and S. P. Morgan, "Optimum design of directive antenna arrays subject to random variations," *Bell Syst. Tech. J.*, vol. 34, pp. 637–663, May 1955.
[31] J. Rissanen, "Modeling by shortest data description," *Automatica*, vol. 14, no. 5, pp. 465–471, 1978.
[32] H. Akaike, "A new look at the statistical model identification," *IEEE Trans. Autom. Control*, vol. 19, no. 6, pp. 716–723, Dec. 1974.
[33] R. R. Nadakuditi and A. Edelman, "Sample eigenvalue based detection of high-dimensional signals in white noise using relatively few samples," *IEEE Trans. Signal Process.*, vol. 56, no. 7, pp. 2625–2638, Jul. 2008.
[34] S. Kritchman and B. Nadler, "Non-parametric detection of the number of signals: Hypothesis testing and random matrix theory," *IEEE Trans. Signal. Process.*, vol. 57, no. 10, pp. 3930–3941, Oct. 2009.
[35] K. Han and A. Nehorai, "Wideband Gaussian source processing using a linear nested array," *IEEE Signal Process. Lett.*, vol. 20, no. 11, pp. 1110–1113, Nov. 2013.
[36] M. Wax and T. Kailath, "Detection of signals by information theoretic criteria," *IEEE Trans. Acoust., Speech, Signal Process.*, vol. ASSP-33, no. 2, pp. 387–392, Apr. 1985.
[37] K. E. Wage and J. R. Buck, "Performance analysis of dominant mode rejection beamforming," in *Proc. Int. Congr. Acoust.*, Sydney, Australia, Aug. 2010, pp. 1–6.
[38] S. M. Kay and S. L. Marple, "Spectrum analysis—A modern perspective," *Proc. IEEE*, vol. 69, no. 11, pp. 1380–1419, Nov. 1981.
[39] M. S. Bartlett, "Periodogram analysis and continuous spectra," *Biometrika*, vol. 37, no. 1/2, pp. 1–16, 1950.
[40] B. F. Cron and C. H. Sherman, "Spatial correlation functions for various noise models," *J. Acoustical Soc. Amer.*, vol. 34, no. 11, pp. 1732–1736, 1962.
[41] W. A. Kuperman and F. Ingenito, "Spatial correlation of surface generated noise in a stratified ocean," *J. Acoustical Soc. Amer.*, vol. 67, no. 6, pp. 1988–1996, 1980.
[42] M. J. Jacobson, "Spacetime correlation in spherical and circular noise fields," *J. Acoustical Soc. Amer.*, vol. 34, no. 7, pp. 971–978, 1962.
[43] H. Cox, "Spatial correlation in arbitrary noise fields with application to ambient sea noise," *J. Acoustical Soc. Amer.*, vol. 54, no. 5, pp. 1289–1301, 1973.
[44] K. M. Cipolla and W. L. Keith, "Measurements of the wall pressure spectra on a full-scale experimental towed array," *Ocean Eng.*, vol. 35, no. 10, pp. 1052–1059, 2008.
[45] R. Bautista, "Performance prediction of coprime sampled arrays in spatially correlated noise," Master's thesis, Univ. Massachusetts Dartmouth, North Dartmouth, MA, USA, Aug. 2017.
[46] C. Therrien, *Discrete Random Signals and Statistical Signal Processing*. Englewood Cliffs, NJ, USA: Prentice-Hall, 1992, ch. 6.2, pp. 301–310.
[47] K. S. Miller, *Complex Stochastic Processes: An Introduction to Theory and Application*. Reading, MA, USA: Addison-Wesley, 1974, ch. 3.2. pp. 82–86.
[48] R. Bautista and J. R. Buck, "Processor dependent bias of spatial spectral estimates from coprime sensor arrays," *J. Acoustical Soc. Amer.*, vol. 143, no. 6, pp. 3972–3978, 2018.
[49] M. K. Simon, *Probability Distributions Involving Gaussian Random Variables: A Handbook for Engineers and Scientists*. New York, NY, USA: Springer, 2007.
[50] I. S. Gradshteyn and I. M. Ryzhik, *Table of Integrals, Series, and Products*, 7th ed. Amsterdam, The Netherlands: Academic Press, 2007.
[51] *Goodness-of-Fit Techniques*, R. B. D'Agostino and M. A. Stephens, Eds. New York, NY, USA: Marcel Dekker, 1986.

Radienxe Bautista (M'15), photograph and biography not available at the time of publication.

John R. Buck (SM'13), photograph and biography not available at the time of publication.